Soft Matter

Observation of Intensity Dependent Phase-Separation in Photoreactive Monomer-Nanoparticle Formulations under Non-Uniform Visible Light Irradiation

Journal:	*Soft Matter*
Manuscript ID	SM-ART-05-2020-000922.R1
Article Type:	Paper
Date Submitted by the Author:	26-Jun-2020
Complete List of Authors:	Pathreeker, Shreyas; Syracuse University, Biomedical and Chemical Engineering Chen, Fu-Hao; Syracuse University Biria, Saeid; Syracuse University, Biomedical and Chemical Engineering Hosein, Ian; Syracuse University, Biomedical and Chemical Engineering

SCHOLARONE™
Manuscripts

Observation of Intensity Dependent Phase-Separation in Photoreactive Monomer-Nanoparticle Formulations under Non-Uniform Visible Light Irradiation

Shreyas Pathreeker,[1] Fu-Hao Chen,[1] Saeid Biria,[1] Ian D. Hosein[1*]

1. Department of Biomedical & Chemical Engineering, Syracuse University, Syracuse, New York 13244, United States

* idhosein@syr.edu

ABSTRACT

We report observations of photopolymerization driven phase-separation in a mixture of a photo-reactive monomer and inorganic nanoparticles. The mixture is irradiated with visible light possessing a periodic intensity profile that elicits photopolymerization along the depth of the mixture, establishing a competition between photo-crosslinking and thermodynamically favorable phase-separating behavior inherent to the system. In-situ Raman spectroscopy was used to monitor the polymerization reaction and morphology evolution, and reveals a key correlation between irradiation intensity and composite morphology extending the entire depth of the mixture, i.e. unhindered phase-separation at low irradiation intensity and arrested phase-separation at high irradiation intensity. 3D Raman volume mapping and Energy Dispersive X-ray mapping confirm that the intensity-dependent irradiation process dictates the extent of phase separation, enabling single-parameter control over phase evolution and subsequent composite morphology. These observations can potentially enable a single-step route to develop polymer-inorganic composite materials with tunable morphologies.

INTRODUCTION

Polymer-nanoparticle composites are a critical materials class that synergizes the benefits of both the polymer (as the matrix) and nanoparticle (as a filler) compositions to provide enhanced properties, such as for optics, mechanics, conductivity, magnetism, thermal stability, anti-wetting, and biomedical applications.[1] Critical to their suitability for applications is the capability to control and tailor their morphology and structure towards accessing key process-structure-property relationships. Preparing polymer-nanoparticle composite materials from photo-reactive formulations of photo-monomer/photo-polymer and nanoparticles is a straightforward, rapid, low-cost, low-energy, and non-destructive approach,[2] in addition to radiation curing being a well-established approach to process materials for a variety of applications.[3] Towards controlling and directing morphology, spatially or temporally periodic as well as non-uniform irradiation profiles have been employed, whereby the underlying gradients in polymerization rate elicit diffusion and dynamic transport processes as well as spatially and temporally evolving mixing instabilities, which lead to spatial organization of polymer and nanoparticle components. Previous examples include lithographic patterns[4-5] and holographic fields.[6]

In both photo-reactive polymer formulations and photopolymer-nanoparticle mixtures, transmitted light patterns have been observed to not diverge as they pass through the medium, rather their spatial profiles are preserved.[7-9] This occurs because of a dynamic balance between a polymerization-induced self-focusing nonlinearity and natural light divergence, in a process referred to as light self-trapping.[10-11] This nonlinear phenomenon is particularly elicited under relatively low light irradiation intensities (~10 mW/cm^2) vs. the generally high photo-curing intensities (~1 W/cm^2) employed in radiation processing.[7] In the former case, rises in the refractive index of the polymerizing medium are slow enough to in turn modulate the propagation path and thus the spatial profile (i.e., suppress divergence) of light. Thereby, when a photo-reactive polymer medium is irradiated with a dim, non-uniform pattern, its spatial intensity profile becomes preserved throughout the entire depth, eventually establishing fixed bright/dark regions that enable reliable control of structure over significantly large thicknesses (>>1 mm). This is unlike traditional uniform irradiation or holographic polymerization, in which the optical fields remain static and unmodified. Irradiation of photo-reactive mixtures with low intensity light in this nonlinear regime has enabled the patterning of polymeric media with thicknesses of several mm to cm, in a process traditionally referred to a projection lithography or light-induced self-writting.[12-14] Thereby, different materials structures have been created such as cross-linked gradients and solvent rich phases,[7, 15] microstructures extracted from the remnant unpolymerized medium,[16-18] different lattice structures,[19-26] coatings,[9, 19, 27] and even micro-fabricated parts.[28]

In binary component systems, such as polymer blends and polymer-solvent mixtures,[29-30] irradiation and consequent self-trapping spatially controls polymerization-induced phase separation (PIPS) such that diffusion is directed in/out of the bright/dark regions, thereby creating structures and morphologies spatially congruent to the light pattern.[10] Through parameters such as irradiation intensity, component weight fractions, and even the light pattern itself,[27, 31-32] photo-crosslinking and phase separation can be balanced so that such congruency with the optical pattern is obtained. These achievements and understanding of patterning and directing phase evolution in multi-component polymer media using self-trapped light patterns now inspires similar investigations in polymer-nanoparticle systems. The significance is in providing a new approach to organize their morphology, reveal more generalized understanding of the process, and provide the opportunity to create new types of structures towards the discovery of new structure-property correlations. Thus far, directing morphology of polymer-nanoparticle systems, beyond uniform irradiation, has been explored using holographic polymerization, which shows the transport of nanoparticles out of irradiated regions.[6, 33]

In this report, we investigate the evolution of morphology in a model system of photo-reactive formulations of a trifunctional monomer (cross-linker) and silicon nanoparticles that are irradiated with a spatially periodic light profile under intensities that elicit light self-trapping. The key motivation to use Silicon nanoparticles is its functionality as a semiconductor as well as a potential anode in Li-ion batteries, keeping future studies in mind. Additional benefits to using Silicon are its high solubility parameter as well as the scarcity of similar studies in the literature that used Silicon. We reveal intensity-dependent morphology, as intensity controls the varying rates of photo-crosslinking and phase separation. Scheme 1 shows the general approach of the irradiation setup, consisting of LED light passed through a photomask (which patterns the light source) then through the photomonomer-nanoparticle formulation. We expect to achieve intensity-dependent morphology based on the rate of photopolymerization (and photo-crosslinking) being intensity dependent,[16, 34-35] which either allows the nanoparticles to (i) at low intensities, phase separate into the non-irradiated (dark) regions of the formulation, or (ii) at high intensities, become trapped in a more rapidly crosslinking polymer matrix (in the irradiated, bright regions). Thereby, we produce structures in 1 mm thick formulations that, respectively, consisting of either a phase separated nanoparticle rich matrix with depleted centers or densely populated vitrified nanoparticle regions, as illustrated in Scheme 1. Hence, varying irradiation intensity within the range that also allows for self-trapping is a promising route to directing the morphology of thick polymer-nanoparticle composite materials.

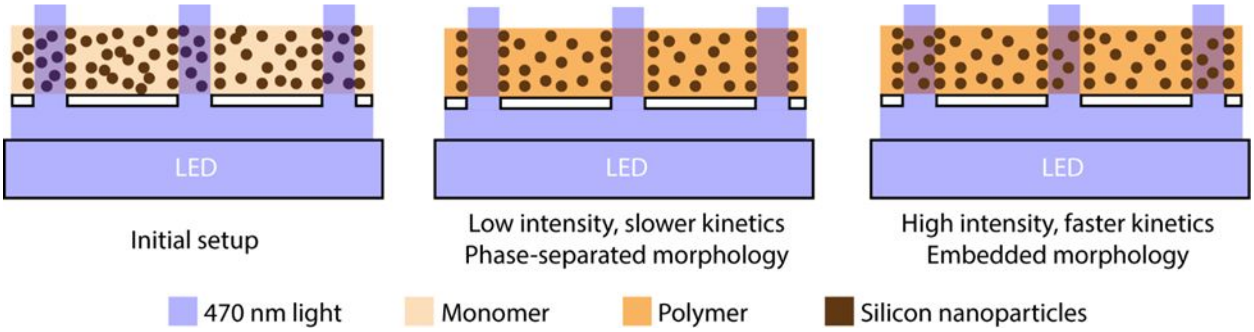

Scheme 1: Illustration of the morphologies expected with variation in irradiation intensity. The setup consists of upward irradiation of a photomonomer-nanoparticle mixture with a periodic array of optical beams generated from an LED. Under low intensity, polymerization-induced phase separation allows the nanoparticles of migrate out of the irradiated regions. Under high intensity, phase separation in inhibited owing to fast polymerization kinetics that inhibit nanoparticle migration.

EXPERIMENTAL METHODS

Materials. Trimethylolpropane triacrylate (TMPTA) monomer, Camphorquinone (CQ) photoinitiator and Silicon nanoparticles (SiNPs) (~90 nm) were all purchased from Sigma-Aldrich, USA. All chemicals were used as received.

Formulations. Photoreactive blends were prepared by dissolving 1.25 wt. % CQ in TMPTA, followed by dispersing 0.1 wt. % SiNPs in the CQ-TMPTA mixture. This mixture was then stirred in the dark for 24 hours to prevent exposure to ambient light.

Irradiation. Irradiation was carried out by shining blue light (λ_{max} = 470 nm) from a collimated LED into homemade cells filled with the photoreactive mixture, as described previously.[16] Briefly, the cells were prepared by attaching one end of a Teflon ring (17 mm diameter) to a glass slide and the other end left open to the atmosphere. The thickness of the cell was fixed at 1 mm, which sets the sample thickness and path length of the transmitted beam. To create a periodic light intensity profile, the LED light was first passed through a chrome mask (Photosciences Inc.) consisting of a square array of apertures 40 μm in diameter and spaced 200 μm apart. This essentially creates an array of 40 μm diameter light beams that subsequently propagate through the mixture. A schematic of the photopolymerization reaction is provided in Supporting Information.

In Situ Raman Spectroscopy. Raman spectra of mixtures under irradiation were acquired using a confocal Raman microscope (Renishaw, inVia) with a 532 nm continuous wave (CW) diode laser.[8] The system combined the Raman spectrometer and a Leica DM2700P microscope. The mixtures were irradiated with LED light from below and probed with the confocal Raman laser from above. The laser spot-size was ~1.6 μm (shown in Supporting Information). Spectra collected over time consisted of line scans over the depth of the mixtures acquired along the central axis of a beam's path length at a step interval of 50 μm, using the automated x, y, z translation stage of the Leica microscope (z-direction). See Supporting Information for a schematic of the setup. A single scan was acquired in ~10 s (collection time for each spectrum was 1 s), and scans were collected over 12 hours at an interval of 5 minutes. No damage from the laser beam was observed in samples over the duration of experiments. TMPTA conversion was calculated based on the carbonyl peak centered at ~1721 cm^{-1} due to its efficacy in tracking conversion of polyfunctional acrylates.[9, 18] Decreases over time in the peak intensities of C=O were used to calculate the local conversion (*p*) and degrees of polymerization (*N*). The conversion was determined by $p = 2(I_0 - I)/fI_0$ where I_0 is the peak intensity at t = 0 min, I is the peak intensity at any time thereafter, and f is the number of functions on the molecule (3 for TMPTA). The degree of polymerization (*N*) was determined from *p* using Carothers' equation.[19] Raman volume images (i.e., 3D maps) of the final morphology were created by acquiring spectra at multiple positions in a sample (with 10 μm step size) using the automated translation stage of the microscope (x, y, and z directions), as described elsewhere.[9, 11, 20]

Characterization. Optical microscope images of photo-polymerized samples were acquired using a Zeiss Axioscope equipped with an Axiocam 105 color camera operated by Zeiss imaging software. Images were captured under transmission mode. Scanning electron microscope images were acquired using a JEOL JSM-IT100LA instrument equipped with an EDS detector. Imaging was carried out at an accelerating voltage of 3 keV, and EDS mapping was carried out at 5 keV. Samples were washed with water and ethanol prior to imaging to remove remnant monomer.

RESULTS AND DISCUSSION

Principles for Intensity-Dependent Control of Photo-Monomer-Nanoparticle Formulations

Light intensity is responsible for free-radical production whose rate of generation (r_a) under conditions of irradiation from one side and oxygen exposure from the other side (ambient) may be expressed as:[16, 36]

$$r_a = \varphi \ln(10)\varepsilon[\mathrm{PI}]\frac{\lambda}{hcN_A}I_0 \exp(-\ln(10)\varepsilon[\mathrm{PI}]z) \qquad (1)$$

where z is the dimension along the propagation length of light, φ is the quantum yield of the photo-initiator, ε is the molar extinction coefficient of photoinitiator at 470 nm, [PI] is the concentration of the photo-initiator, λ is the wavelength, I_0 is the incident light intensity, h is Planck's constant, c is the light speed, and N_A is Avogadro's constant. Specifically, the straightforward linear relation $r_a \sim I_0$ is the principle by which we can rationally tune the photo-initiation kinetics as an approach to control polymerization and consequent morphology evolution with growing molecular weight. The rise the polymer refractive index (Δn) is also related directly to intensity and photo-initiation and implicitly to polymer molecular weight by:[37]

$$\Delta n(x,y,z,t) = \Delta n_s \left\{1-\exp\left[-\frac{1}{U_o}\int_0^{t-\tau} |E(t')|^2\, dt'\right]\right\} \qquad (2)$$

where Δn_s is the maximum achievable index change (between fully cured and uncured photopolymer media), U_0 is a critical energy density to initiate free-radical polymerization (units of J/cm^2), τ is the monomer radical lifetime, and $|E(t)|^2$ is intensity. Equation 2 correlates rise in refractive index specifically to the integrated intensity over time, the efficiency/rate of the photopolymerization reaction, as well as the polymer structure associated to Δn_s. We have previously shown that intensities between ~4-20 mW/cm^2 allow light to undergo self-trapping, so we eliminate any intensity dependence to the optics of the process. Rather we expect intensity to only vary the underlying photopolymerization kinetics. The rise in polymer molecular weight stimulates mixture instability and the onset of phase separation in accordance with the change in the total Gibbs free energy of the system:[38-39]

$$\frac{\Delta G}{RT}=\frac{3}{2N_1}\left(\varphi_s^{2/3}\varphi^{1/3}-\varphi\right)+\frac{2\varphi}{fN_1}\ln\left(\frac{\varphi}{\varphi_s}\right)+\frac{(1-\varphi)\ln(1-\varphi)}{N_2}+\chi\varphi(1-\varphi)\quad(3)$$

where φ is the volume fraction of acrylate, φ_s the network volume fraction, N_1 and N_2 the degrees of polymerization for the monomer and nanoparticle (N_2 = 1), respectively, f the functionality of TMPTA, and χ the interaction parameter. The critical interaction parameter, χ_c, indicates the point at which spontaneous phase separation occurs, and is determined by when the second derivative of the free energy is zero:

$$\chi_c=\frac{1}{2}\left(\frac{2}{fN_1\varphi}+\frac{\varphi_s^{2/3}}{N_1\varphi^{5/3}}+\frac{1}{N_2(1-\phi)}\right)(4)$$

As χ_c decreases with increases in N_1 over time, the onset of mixing instability is indicated by when $\chi_c < \chi_{FH}$,[40] where χ_{FH} is the Flory-Huggins interaction parameter of the mixture determined by the Hildebrand solubility parameters (δ) of the components:[40]

$$\chi_{FH}=\frac{V_r}{RT}(\delta_1-\delta_2)^2\qquad(5)$$

The calculated χ_{FH} of the TMPTA-Silicon nanoparticle system was 8.8, using solubility parameters for TMPTA and silicon found elsewhere.[29, 41]

Phase separation is expected in such high χ polymer-nanoparticle mixtures owing to their chemical dissimilarity. Furthermore, the radius of gyration R_g of TMPTA was calculated (See Supporting Information) to be ~0.54 nm whereas R_{Si} of the Silicon nanoparticle was ~45 nm, placing the system in the colloidal limit,[26] wherein $R_{Si} >> R_g$ and phase-separation is naturally expected due to the large mismatch in radii and the consequent entropic penalty experienced by polymer chains in order to accommodate the large nanoparticles at the expense of the freedom to explore a greater configurational space. Furthermore, several other studies, both theoretical and experimental, have reported that the inorganic phase dispersed in a polymer matrix would tend to phase-separate out into monomer-rich regions.[42-47] The depletion attraction theory is widely acknowledged to be the actual mechanism responsible for phase-separation in such systems, wherein the particles experience an attractive force between one another, leading to aggregation and consequently, phase-separation.[47] Similar phase-separation phenomena have also been observed in semiconductor nanocrystals and nanorods.[4-5] Hence, we expect such systems, while thoroughly mixed, to be in an inherently unstable state, and photo-polymerization and photo-crosslinking can either facilitate (driving greater chemical potentials that drive diffusion) and/or inhibit phase separation (increasing system viscosity and elasticity that arrests diffusion). Equation 4 illustrates the inherent competition in the system based on the molecular weight, N_1, of TMPTA. As it increases, the decrease in χ_c eventually favors phase separation. Photo-crosslinking is indicated in the equation to some extent by f, and by varying the relative weight fraction of the polyfunctional. However, the relative weight fractions are kept constant herein at 0.1 wt % SiNPs.

In-situ Tracking of Conversion and Silicon Intensities

Figure 1a shows TMPTA conversion over an irradiation period of 12 hours at 4 mW/cm^2. Maximum double bond conversion of ~35% is achieved within the first 2 hours of exposure, beyond which there is nearly no increase (data for other depths are shown in Supporting Information). This behavior is attributable to the formation of a cross-linked polymer network, which traps monomer, free radicals, and oligomer, rendering the system diffusion limited, in what may be referred to as a gel-sol medium expected at this level of conversion.[48] As such, no further conversion of monomer occurs even though the gel-like network likely contains monomer molecules available to partake in the polymerization reaction. This gel-point plays an important role in determining whether a system undergoes phase-separation since it is directly associated with mobility of the components in the polymerizing medium. Attainment of the gel-point during the polymerization of multifunctional monomers has been associated with a critical conversion of between 25% and 35% both theoretically and experimentally.[49-50] Moreover, dominance of the termination reaction has also been reported to begin at low monomer conversion for TMPTA,[51] which limits any further monomer conversion thereafter. Although we do not directly characterize the gel-point, it would be reasonable to conclude by comparing our data to the literature that the gel-point in our system is attained at a conversion of ~25%, which corresponds to an exposure time of ~60 minutes. Figure 1b shows Si intensities for the same irradiation time, over which we observed that Si intensities decrease across all depths, indicating decrease in local Si concentration.[8]

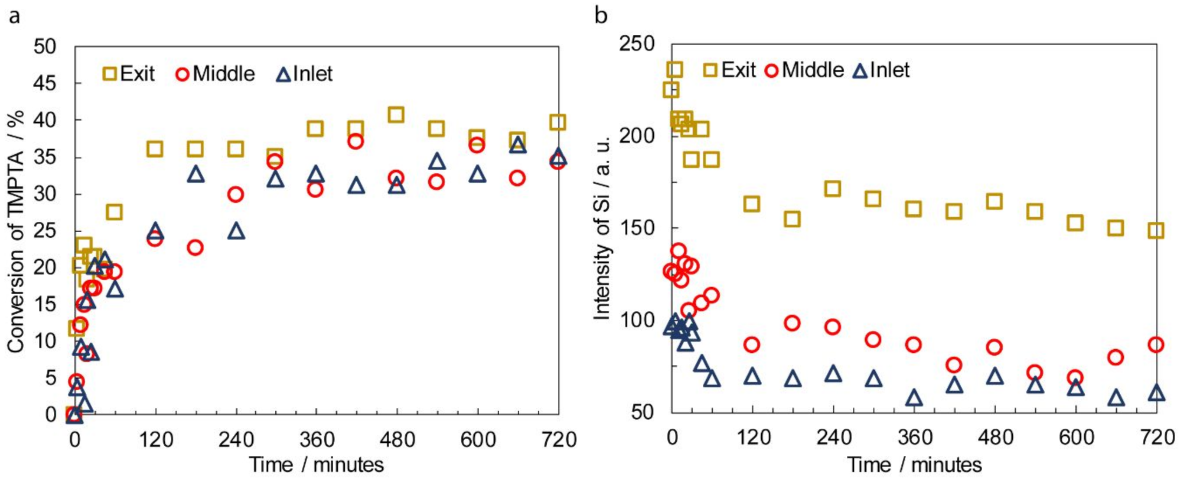

Figure 1. (a) TMPTA conversion and (b) Silicon Raman peak intensity over irradiation time at the top surface, middle, and the bottom surface of a channel, the latter of which corresponds to the inlet plane of the light. Exposure intensity was 4 mW/cm^2.

Remarkably, Si intensities only decrease until about 60 minutes after exposure, which coincides well with the gel-point discerned based on monomer conversion data. Si intensities at the greatest depth in the mixture do appear to be higher, possibly due to absorption and scattering of the laser light by the Si nanoparticles, which has been previously show to have absorbances at ~500 and 800 nm,[52-53] as thus not a significant contribution an attenuation of the process. Also, scattering of light by SiNPs is not deleterious to the self-trapping process.[8-9] It is possible owing to greater polymerization rate at shallower depths that in addition to loss of silicon in the irradiated region, that there is also a superimposed transport of particles to greater depths, away from the shallower regions (close to the entrance of light into the sample) that are more polymerized. However, the decreasing trend in Si intensities prevails across all depths over (data for other depths shown in Supporting Information). This indicates that the general direction of phase separation is coaxial to the cylindrically irradiated regions, with SiNPs diffusing into the dark regions. Beyond 60 minutes, Si intensities remain invariant, indicating arrest of phase-separation. This observation can be attributed to the above-mentioned gel-like network, which characteristically prevents bulk diffusion in the medium.

Hence, reaction kinetics and thermodynamics both play important roles in phase-separation, but control over the phase-separation process can be exercised by varying the reaction kinetics.[8] We investigated the influence of light intensity on the phase-separation process, results for which are shown in Figure 2. Figure 2a shows monomer conversion at an irradiation intensity of 20 mW/cm^2. Although the resolution within the first 60 minutes is low, it is evident that monomer conversion increases rapidly to ~25% within the first 15 minutes and plateaus thereafter. Based on the arguments made previously, it can be concluded that gelation occurs within 15 minutes at high intensity. Acceleration of gelation at higher irradiation intensity is expected due to increased photo-initiation and propagation, and a decrease in time to gelation with increase in irradiation intensity has been reported previously,[23] with a decreased time to gelation also directly being associated with the inability of a system to phase-separate.[24]

In contrast to low intensity irradiation, data for high intensity irradiation would indicate that the onset of gelation precedes any observable phase-separation in this case. As evidence, in contrast to the decrease in Si intensities observed for samples irradiated at 4 mW/cm^2 as shown in Figure 1b, Si intensities for samples irradiated at 20 mW/cm^2 initially appear to increase slightly, but remain unchanged thereafter across all depths (Figure 2b). The increase in intensity may be attributed to densification of the medium with curing. Although in a such high χ-systems phase-separation is favorable, at higher irradiation intensity it can be inferred from the data that the rate of polymerization achieves a level of molecular weight and crosslinking to inhibit the thermodynamically favorable drive for phase-separation, consequently trapping nanoparticles within the irradiating paths of the optical beams due to the rapid formation of a gel-like network. While the entire mixture undergoes gelling, it is likely that the sample has a gradient crosslink structure, owing to the greater polymerization rate in the irradiated region, and the dark regions polymerize more so from diffusion of free-radicals.[7, 16]

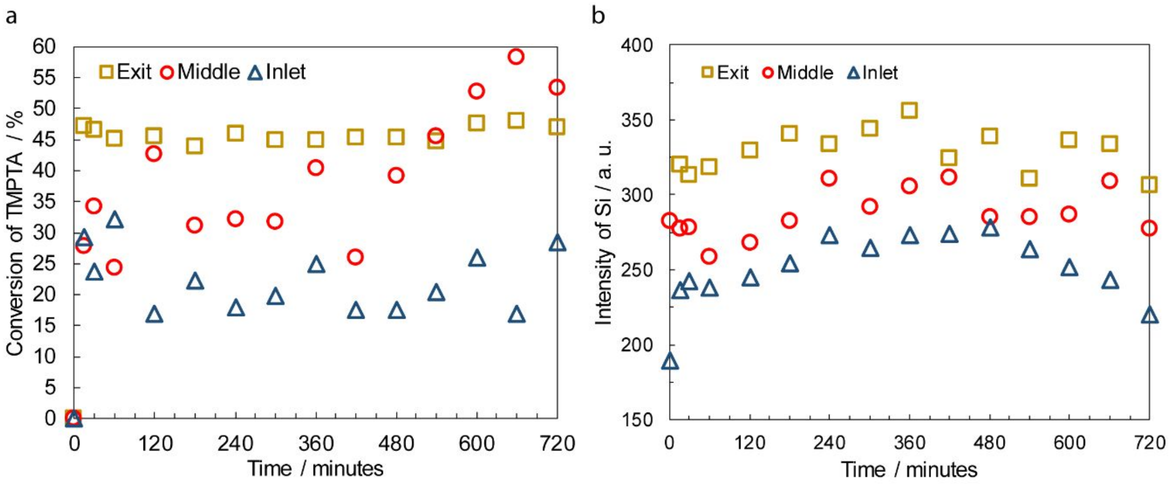

Figure 2 (a) TMPTA conversion and (b) Silicon Raman peak intensity over irradiation time at the top surface, middle, and the bottom surface of a channel, the latter of which corresponds to the inlet plane of the light. Exposure intensity was 20 mW/cm^2.

While magnitudes of monomer conversion are in a comparable range for both irradiation intensities, magnitude of Si intensities at 20 mW/cm^2 are higher than those at 4 mW/cm^2 although identical resin mixtures were used for all experiments. These data (data for other depths provided in Supporting Information) confirm that a higher degree of phase-separation can be achieved at low irradiation intensity, which in-turn points to the ability to control morphology in such nanoparticle-monomer mixtures. Monomer conversion at the inlet face appears to saturate at ~25% whereas that towards the exit face appears to be higher. A plausible explanation is the difference in viscosity of the medium between the bottom and top surfaces of the samples. Rapid monomer conversion near the inlet face renders that region highly immobile and therefore, saturation in conversion is reached. Towards the exit face, however, polymerization proceeds as radicals and monomer molecules are still sufficiently mobile to participate in the polymerization reaction, leading to increased conversion. It should also be noted that in our in-situ setup, acquisition of spectra at the bottom surface lags acquisition at the top, and given this lag, some irregular behavior maybe expected. Nonetheless, we believe that there is sufficient contrast between the two in-situ data to permit comparison of the extent of phase-separation. (Depth scan of samples before polymerization, representative Raman scans before and after polymerization, as well as calculations of degree of conversion can be found in Supporting Information).

Correlating Polymerization Kinetics to Thermodynamic Mixing Instability and Diffusion

The Si Raman intensities provide evidence for the phase separation of SiNPs out of the irradiated regions. To further the analysis, we assessed the rates of conversion and tracked the theoretical thermodynamic stability of the mixtures to correlate them to this change in SiNP concentration. Figure 3 shows calculated conversion rate and rates of polymerization (Rp) versus conversion and time for samples irradiated at 4 and 20 mW/cm^2. At low intensity, we observe that maximum conversion is attained after 20 minutes of exposure, whereas at high intensity rapid monomer conversion occurs attaining a maximum within 15 minutes of exposure (Figure 3a), clearly showing the accelerating effect of high irradiation intensity on the photopolymerization reaction. After reaching their maximum there is a sharp drop with rates to ~0. The maxima and subsequent decline in rates of conversion shown in Figure 3a are characteristic of the Tromsdorff-Norrish effect as expected with polymers that possess a T_g greater than the experimental temperature. Figures 3b and Figures 3c show polymerization rates as a function of monomer conversion and exposure time, respectively. In all plots, polymerization rate initially increases rapidly, reaching a maximum and then drastically falling thereafter, exhibiting the classical auto-acceleration and auto-deceleration like behavior,[54-56] which accelerates the rise in molecular weight that can either drive phase separation or inhibit it, depending on the amount of time available for the SiNPs to diffuse out of the irradiated regions. Maximum rates of polymerization are attained sooner at higher light intensity than at low light intensity, i.e. 15 minutes versus 20 minutes, thereby affording an additional 5 minutes at low light intensity for reaction and diffusion dynamics to proceed, which is significant because nanoparticle transport would be expected within this time, owing to the onset of instability of the sample. Attainment of $R_{p\text{-}max}$ appears to occur at higher monomer conversion (~28%) at high light intensity, yet at lower monomer conversion (~16%) at low light intensity. Although apparently anomalous, such behavior has previously been reported due to a delay in the rate of volume shrinkage at high light intensity, which increases overall free volume and consequently, mobility.[54] While this phenomenon could be responsible for the increased monomer conversion observed at higher light intensity, diffusion of particles in this regime would be highly improbable owing to their large size. Moreover, increased cross-linking attributed to higher conversion at high irradiation intensity would also contribute to retardation of particle dynamics, if at all any. This rapid increase in the rate of conversion leads to a rapid decrease in the χ_c of the system (Figure 4), meeting conditions for mixing instability ($\chi_c < \chi_{FH}$) at approximately 15 and 20 minutes for 4 mW/cm^2 and 20 mW/cm^2, respectively. Yet, while thermodynamically unstable, the spectroscopic and conversion data point inability for the SiNPs to diffuse out of the irradiated region in the system irradiated at 20 mW/cm^2, indicating an arrested state to the morphology.

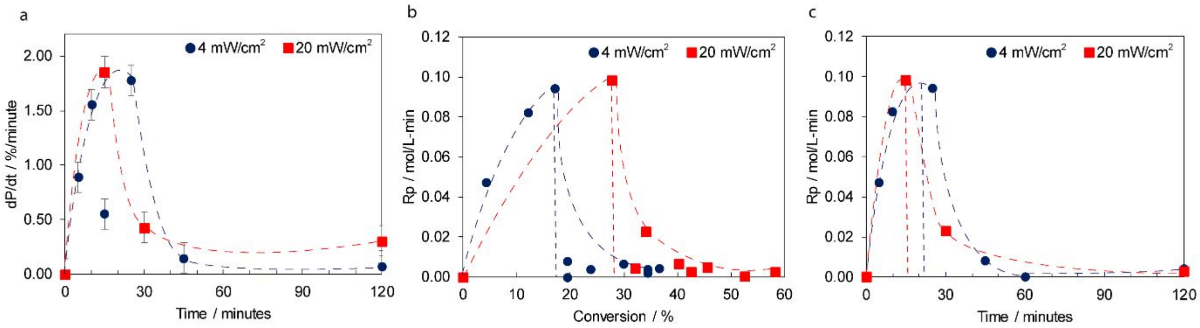

Figure 3. Polymerization kinetic data. (a) Conversation rate over time. (b) Rate of polymerization versus conversation. (c) Rate of polymerization over time. Vertical dashed lines in (b) and (c) indicate points at which maximum polymerization rate occurs.

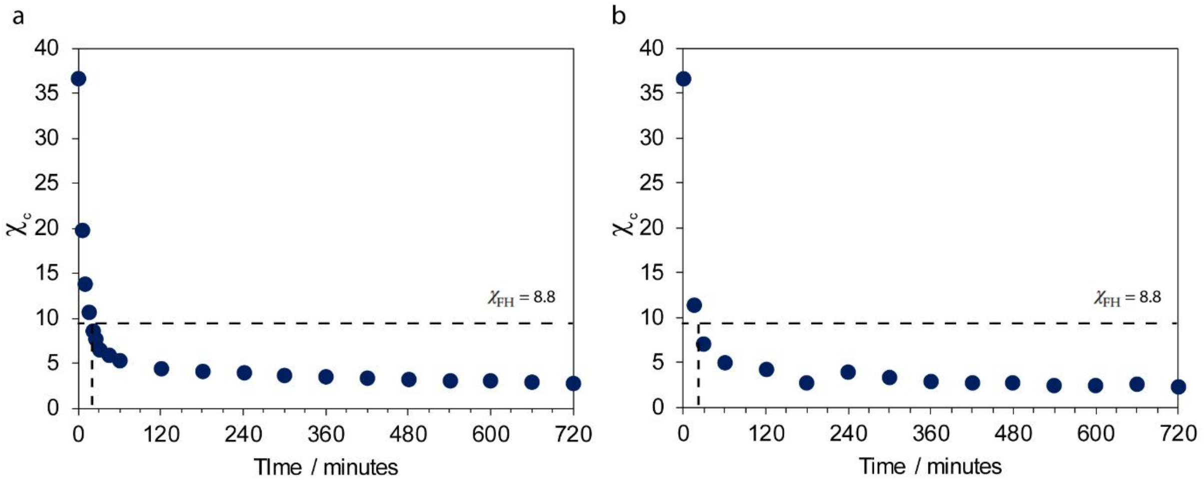

Figure 4. Change in χ_c as a function of irradiation time and intensities of (a) 4 mW/cm^2 and (b) 20 mW/cm^2.

To more closely relate the onset of phase separation to the diffusion capabilities of the nanoparticle, we calculated both the system viscosity and nanoparticle diffusion constant. The intrinsic medium viscosity can be correlated to the polymer molecular weight using the Mark-Houwink equation:[57]

$$[\eta] = KM^a \qquad (6)$$

Where, a and K are parameters characteristic to the system, and M is the polymer molecular weight. In this study, we assumed a value of 0.8 for a and calculated K using the initial viscosity and molecular weight of the TMPTA monomer. Owing to the lack of dynamic rheological or fluorescence correlation measurements to determine bulk viscosity during polymerization (measurements for which are planned for future studies) we approximated that the bulk viscosity $\propto$ 9 times the intrinsic viscosity estimated using the Billmeyer[58] and Solomon-Ciuta[59] relations. These bulk viscosity values were then used to estimate diffusion coefficients to correlate viscosity with diffusivity. Another assumption made for the purpose of this estimation was that the viscosity average molecular weight M_v = M_w. M was calculated using Carother's equation as shown in Supporting Information. The a parameter is generally around 0.7 for linear polymers,[60] but a slightly higher value was used in this work owing to the branched nature of TMPTA. Although no solvent was used in our work, we employed the good solvent approximation in selecting a suitable Mark-Houwink-Sakurada exponent 'a' owing to the presence of Silicon nanoparticles in the mixture. It can be imagined that the particles swell the monomer segments, thereby to some extent satisfying the conditions characteristic of a good solvent system. Furthermore, the choice of the assumed exponent is reasonable as it is similar to that other acrylates such as PMMA (0.7) while accounting for the branched and relatively more rigid nature of TMPTA. Lastly, the low Silicon concentration allows use of the Stokes-Einstein equation to estimate diffusion coefficients. The diffusion coefficient (D) can be determined reliably in the large particle limit using the Stokes-Einstein equation:[61-63]

$$D = \frac{k_B T}{f \pi \eta R} (7)$$

Where, k_B is the Boltzmann constant, T is the ambient temperature in Kelvin, f is related to the stick boundary condition,[64] η is the bulk viscosity of the medium, and R is the radius of the particle. Figure 5 shows plots of diffusivity and rate of diffusion over irradiation time for both irradiation intensities explored. The diffusivity drops faster and to a larger extent in samples irradiated at 20 mW/cm^2. Likewise, rates of diffusion in peak and drop off earlier in a sample irradiated with higher intensity. This data indicates that diffusion of the particles at lower irradiation intensity as extends for a longer duration, which in turn can explain the ability for there to be drops of SiNP concentration in the irradiated region.

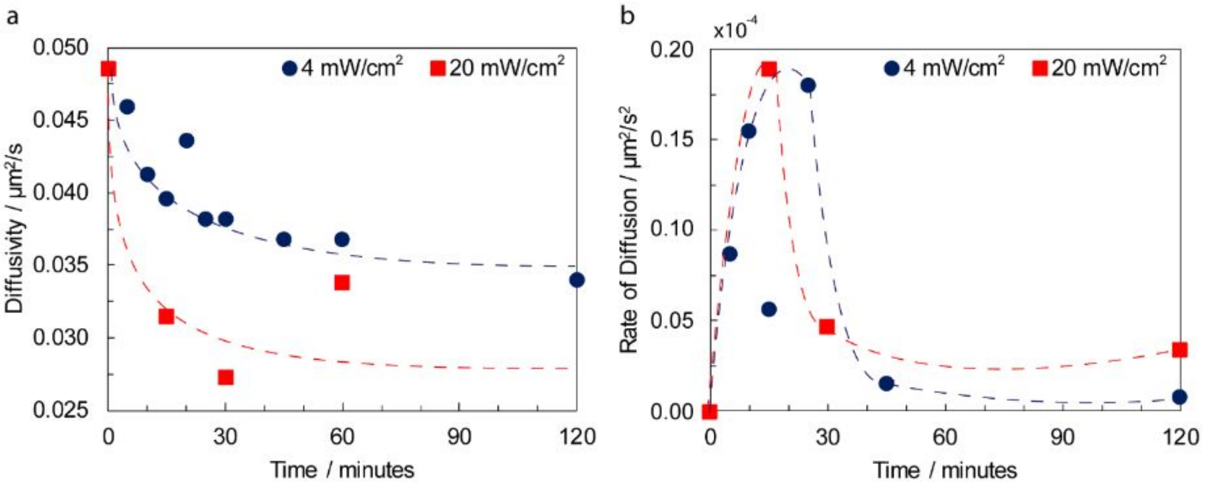

Figure 5. Plots of (a) Diffusivity and (b) rate of diffusion over time.

3D Raman Volume Mapping of Morphologies

The kinetic and thermodynamic data provide experimental and theoretical rationale for the expulsion of SiNPs from the irradiated regions, a phenomenon that is clearly correlated to irradiation intensity and capability to vary the internal polymerization rates, particle diffusion and mixing instability, particular over time. While in-situ spectroscopic experiments provide insight into the influence of irradiation intensity on the extent of phase-separation, we also investigated the final morphology of the structures using ex-situ Raman volume mapping. Moreover, in-situ experiments were conducted on a film of the mixture whereas ex-situ characterization was performed on cured samples prior to which uncured monomer was washed away using ethanol. This is the reason cross-sectional images show pillar-like structures. We have previously reported the use of 3D Raman volume maps to characterize polymer morphologies.[9] Briefly, multiple point spectra collected in a defined volume of the sample are integrated to develop a contrast map based on the desired characteristic Raman peak position of the components (i.e. ~521 cm^{-1} for Silicon and ~1721 cm^{-1} for C=O representing TMPTA). The in-situ experiments were designed to monitor variation in Raman peaks to determine monomer conversion, whereas ex-situ Raman mapping presents a picture of the final morphology based on the presence of remnant reactant materials, in this case TMPTA composition is mapped using the C=O bond as representative of its location. The idea of presenting 3D Raman maps generated are not to further investigate monomer conversion and reaction kinetics, but rather to inform on the final distribution of components in the system, importantly with regards to the SiNPs.

Figure 6 shows cross-sectional volume maps for TMPTA, Silicon, and a ratio map of Silicon to TMPTA in a single channel irradiated at 4 mW/cm^2. The white lines visually aid in separating the core from its surrounding. The lateral dimension of this core coincides well with the aperture diameter in the photomask used, i.e. 40 μm. Furthermore, the cross-sectional profile of the structure is visible in Figure 6a, which can be confirmed with SEM images provided in Supporting Information. In the maps, bright colors indicate high concentration of a component whereas dark colors represent its deficiency. In Figure 6a, the core region appears C=O rich due to the presence of unreacted TMPTA moieties. This is not a surprising observation and can be explained by the gel-network formation as informed by the in-situ data. Therefore, local immobilization of C=O moieties would likely have occurred within the first 2 hours of exposure until the gel point was reached, beyond which the system becomes diffusion-limited, restricting movement of monomer molecules and free radicals. The Gaussian nature of the light beam is also an important factor contributing to local non-uniformity in curing conditions, i.e. the rate of polymerization would be highest at the center of the core relative to its surrounding. Based on this, we expect a gradient of monomer concentration to be established between the core and its surrounding, which drives diffusion of fresh monomer molecules into the core from its peripheries. In order to sustain the high rate of polymerization in the core, the monomer concentration gradient depletes the surrounding of monomer. The already monomer-depleted volume then undergoes polymerization due to leakage of light and outward diffusion of radicals. This process is what causes the surrounding region to appear C=O deficient. Yet, the key observation here is that due to the geometry of the mask and the intensity profile of the light beam, the rate of polymerization in the core is much higher than that in its surrounding, and the surrounding eventually undergoes polymerization due to the close spacing of light beams (200 μm). To support this hypothesis, we performed a control experiment under the same conditions without a photomask, for which the 3D Raman map clearly reveals uniform curing as the entire film was subject to the same irradiation intensity (See Supporting Information). Figure 6b shows a volume map of Si distribution, wherein a Si depleted core is indicated by the dark blue region is evident. Notably, this observation agrees well with the in-situ data showing Si intensities appeared to decrease over irradiation time. We also note based on this data that the morphology remains unchanged after the gel-point is reached. The rationale behind curing samples for 12 hours was to achieve as high a conversion as possible, which would preclude the possibility of long-term change in morphology occurring with variation in monomer conversion, namely such morphologies are in stationary states. Lastly, the map in Figure 6c shows a mapping of the ratio of Si vs. C=O, which is useful to visualize the relative distributions of components in the sample. The surrounding region is Si-rich, which is expected due to the radially outward movement of SiNPs due to polymerization-induced phase separation. The core appears to be Si-deficient, and further confirms Si phase-separation, thereby revealing a core-shell-like morphology. Full 3D Raman volume maps (non-section) can be found in Supporting Information.

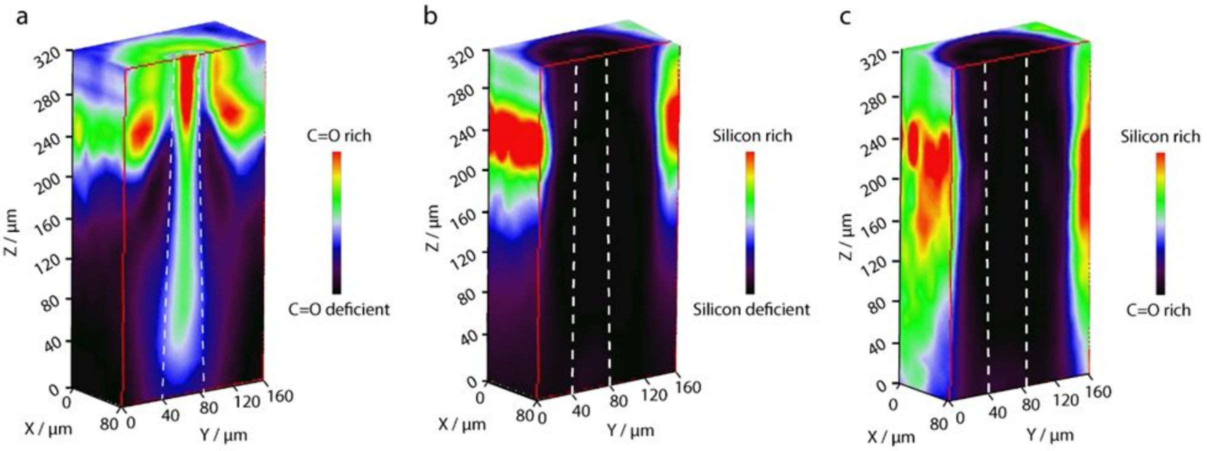

Figure 6. Raman volume maps of a single a single polymerized channel obtained after curing at an intensity of 4 mW/cm^2. Volumes show Raman intensity for (a) C=O, (b) Silicon nanoparticles, and (c) Ratio Si to C=O peak

intensities. All maps are sliced in the yz plane (red outline) to reveal the cross-section of the channel. Dashed lines visually delineate the core from its surroundings.

Figure 7 shows cross-sectional 3D Raman volume maps for a sample cured at an irradiation intensity of 20 mW/cm^2. The lateral dimension of the core indicated by dashed white lines again corresponds well with the aperture of the photomask used (40 µm). In Figure 7a, the lower half of the core appears C=O deficient which is expected due to higher monomer conversion ascribed to the higher light intensity used. The upper half of the core appears rich in remnant C=O, which is likely due to trapping of unreacted monomer. As seen with the low intensity case, the profile of the structure is also visible here, with corresponding SEM images provided in Supporting Information. Figure 7b reveals what appears to be a Si-deficient core, in contrast to the in-situ data which suggested an embedded-type morphology. Figure 7c also appears reveals a core-shell type morphology. To reconcile this difference, we performed quantitative Raman analysis, as all Raman acquisitions were performed under identical conditions, the results for which are tabulated in Table 1. Table 1 shows that C=O Raman intensities in the core region are similar to one another, but Si Raman intensity in the core region at 20 mW/cm^2 is more than double that at 4 mW/cm^2. This feature was observed in the in-situ data, pointing towards the fact that the extent of phase-separation achieved using high irradiation intensity is lower than that at low irradiation intensity. Furthermore, considering the magnitudes of Si/C=O intensities, Si concentration in the core region at 20 mW/cm^2 is much higher than that at 4 mW/cm^2. Given that C=O intensities are comparable for both irradiation intensities, this difference can be attributed to a difference in Si concentrations. Based on this analysis, it can be inferred that a higher degree of phase-separation can be achieved at low irradiation intensity, when compared to high irradiation intensity wherein phase-separation is observed to be arrested to some extent.

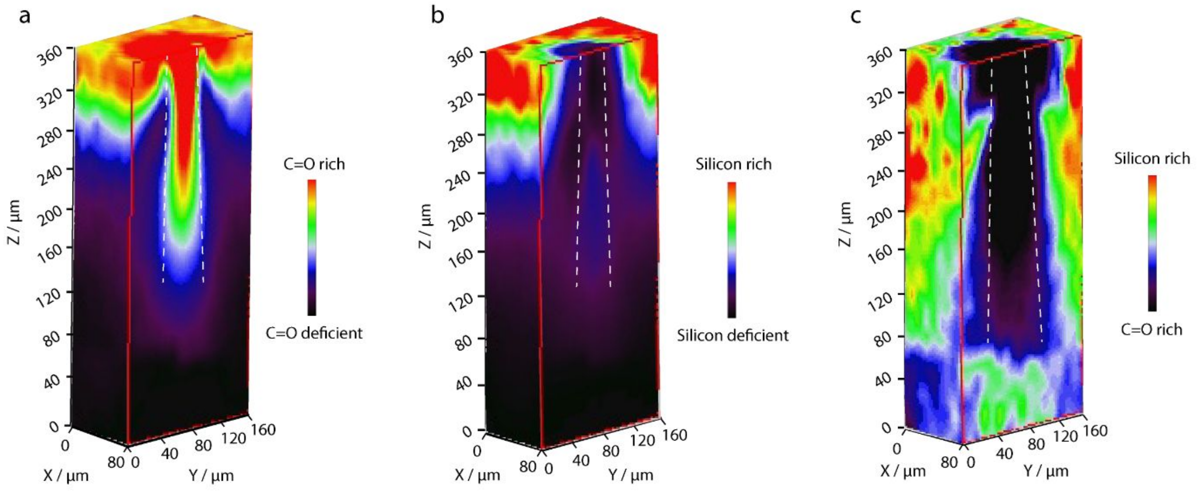

Figure 7. Raman volume maps of a single a single polymerized channel obtained after curing at an intensity of 4 mW/cm^2. Volumes show Raman intensity for (a) C=O, (b) Silicon nanoparticles, and (c) Ratio Si to C=O peak intensities. All maps are sliced in the yz plane (red outline) to reveal the cross-section of the channel. Dashed lines visually delineate the core from its surroundings.

Table 1: Comparison of Silicon and C=O Raman intensities for 4 mW/cm^2 and 20 mW/cm^2

Light Intensity (mW/cm^2)	**C=O$_{core}$ (a. u.)**	**C=O$_{shell}$ (a. u.)**	**Si$_{core}$ (a. u.)**	**Si$_{shell}$ (a. u.)**	**Si/C=O$_{core}$ (a. u.)**	**Si/C=O$_{shell}$ (a. u.)**
4	204.7	1982.2	126.9	5291.7	0.085	5.116
20	115.1	1656.7	319.9	5111.3	1.495	4.110

To further characterize the morphologies obtained, we performed EDS mapping on the samples. Figure 8a shows an optical microscope image of the sample, where a uniform array of periodically spaced structures is clear along with the structures' cylindrical cross-section. For clarity, we hereon use the terms bottom, middle and top, which correspond to the inlet, middle, and exit points of the light beams. Figures 8b, d, and f reveal top-down slices of Raman volume maps of Si at the top, middle and bottom surfaces of the channel, respectively. A core-shell morphology is evident, represented by the dark blue region indicating low Si concentration and the bright green region indicating high Si concentration. On the other hand, Figures 8c, e, and g represent C=O concentrations at the same depths. The top surface consists of more unreacted C=O, the middle appears to consist of reacted and partially unreacted monomer remaining due to entrapment, and the bottom appears completely C=O deficient with the least amount of unreacted monomer, which is expected as this plane corresponds to the inlet face of the light beam. From these Raman slices, it is also noteworthy that the cylindrical cross-section and morphology of our structures is preserved across the entire sample thickness, which points to the benefit of self-trapping to enable a consistent irradiation profile over depth to achieve a relatively uniform morphology pattern from the top to the bottom of the sample. An SEM micrograph of a single structure whose tip (approximately 50 μm tall) was sliced off, is shown in Figure 8h, where in the circular cross-section of the cylindrical channel is clearly visible. Its diameter corresponds well with the aperture of the photomask used, and the circular top-down profile agrees well with the Raman slices shown, indicating uniform morphology across the entire depth. We employed EDS mapping to reveal the spatial distribution of the components, which is an effective way to analyze differences in materials compositions.[37] EDS maps of this region for Si and Carbon are shown in Figure 8i and Figure 8j, respectively. The dark circular region in Figure 8i represents the core of the structure, which is the region of importance in this study. Notably, this region is devoid of Si relative to its surroundings, which corroborates the observations made in the in-situ and ex-situ Raman measurements. Carbon intensity is also lower in the center than in the surroundings, which is owing to a shadowing effect from the location of the EDS detector and the slightly protruding nature of the irradiated region (See Supporting Information). The central region appears dark as the color gradient in the maps is generated based on the number of counts, i.e. regions with more counts are bright whereas those with low counts are dark (see Supporting Information for EDS spectra and mapping conditions). Overall, these results reflect a core-shell type morphology due to polymerization-induced phase-separation, which extends over the depth of the sample, owing to the self-trapping nature of light.

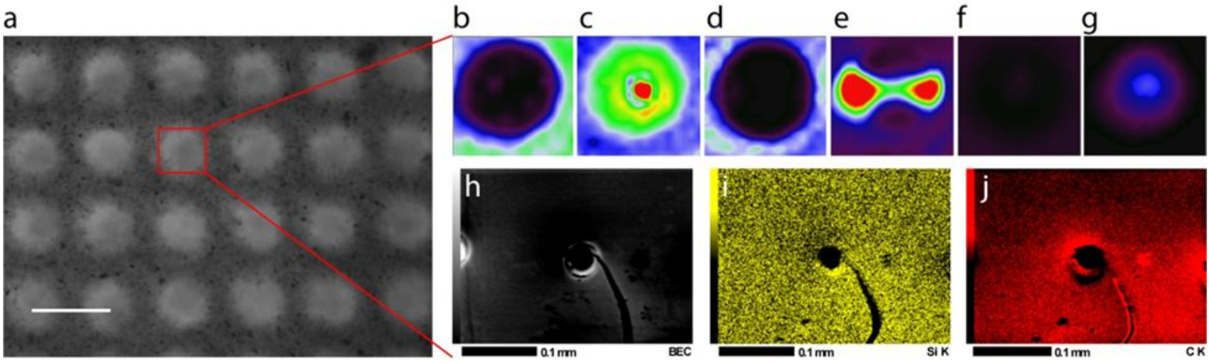

Figure 8. Morphology characterization of channels cured at 4 mW/cm^2. (a) Optical microscope image showing a 2D periodic array of polymerized channels. XY slices of Raman volume maps for (b, d, f) Silicon, and (c, e, g) C=O at depths of 300 μm (b, c), which is the top surface of the channel, 150 μm, which is the middle (d, e), and 0 μm, which is the bottom of the channel (f, g). (h) Backscatter electron microscope image of a single channel whose tip was sliced using a sharp razor blade. EDS maps of (i) Silicon and (j) Carbon performed on the sliced tip. The crack was accidentally formed during handling. Scale bar in (a) is 200 μm.

Figure 9a shows a top-down optical microscope image of a sample cured at 20 mW/cm^2 depicting a similar pattern as shown in Figure 8a. Figures 9b, d, and f reveal top-down slices of Raman volume maps of Si at the top, middle and bottom surfaces of the channel, respectively. In contrast to a clear core-shell morphology, a gradient of Si concentration spanning radially outward from the center is evident in Figure 9b. The middle and bottom of the channel appear to be Si-deficient, but based on quantitative Raman analysis, Si concentration in the core region of the sample cured at 20 mW/cm^2 is higher than that at 4 mW/cm^2. Figures 9c, e, and g represent C=O concentrations at the same depths. Again, the top surface consists of more unreacted C=O, but the middle appears to contain more entrapped monomer relative to 4 mW/cm^2 indicated by the bright green region. The bottom appears to be highly C=O deficient due to high monomer conversion. An SEM micrograph of a sliced structure is shown in Figure 9h, wherein a uniform cross-section is visible along with a thin outer layer of Silicon. Moreover, the cross-sectional profile coincides with the top-down Raman slices shown, again pointing towards a structure that retains its dimensions and profile along its depth. In both cases, the outer surface appears smooth, whereas the underlying composite material consisting of polymer and SiNPs appears rough, which in part may be due to shearing caused during sample preparation. Additional SEM images in cross-section can be found in Supporting Information. The central region in Figure 9i represents the core of the structure. Although this core appears to be devoid of Si relative to its surroundings, quantitative analysis of EDS spectra confirms that it contains approximately 2.5 times more Silicon than 4 mW/cm^2 (see Supporting Information for additional data, including SEM images and EDS maps in cross-section, tabulated EDS intensities and EDS acquisition conditions). Collectively, these results clearly indicate that more Si is present in the core region at high irradiation intensity, and this attributed to the arrest of phase-separation due to fast molecular weight increase associated with the higher irradiation intensity. While these results do not reflect an entirely embedded morphology (i.e., fixed SiNP concentration with no loss in the irradiation region), they do confirm lesser phase-separation at a higher irradiation intensity. Furthermore, higher irradiation intensity has recently been shown to cause arrested phase-separation in a polymer blend,[7] and our results do reveal a similar dependence of phase-morphology on irradiation intensity, but in a composite mixture. Two factors, namely monomer conversion and medium viscosity govern the extent of phase separation. At low light intensity, maximum monomer conversion is low and the rise in viscosity is low owing to slow reaction kinetics. As a result, a longer duration for particle movement is enabled (indicated in Figure 3c) relative to high light intensity. At high light intensity, maximum monomer conversion is higher and the rise in viscosity is also higher, which leads to the arrest of phase-separation dynamics. The Si-depleted and Si-rich regions shown in Figures 8(b, d, f) and 9(b, d, f), respectively, reflect the higher extent of phase-separation at low light intensity and lower extent of phase-separation at high light intensity.

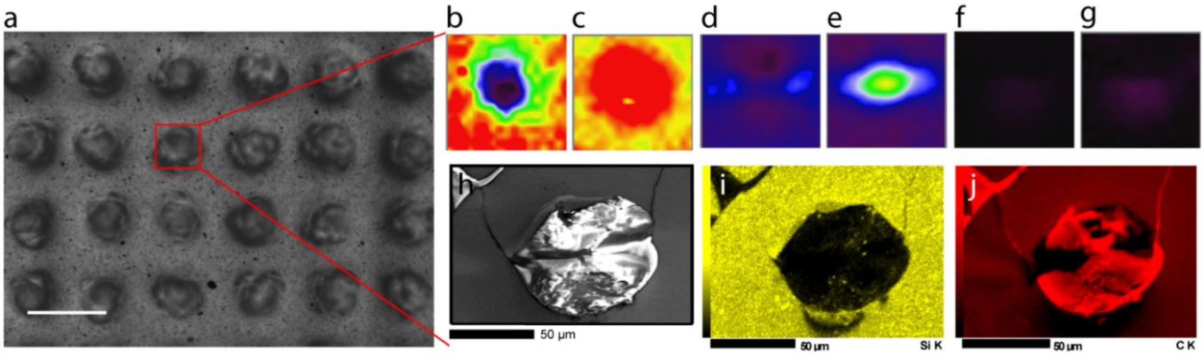

Figure 9. Morphology characterization after curing at 20 mW/cm^2. (a) Optical microscope image showing a 2D periodic array of polymerized channels. XY slices of Raman volume maps for (b, d, f) Silicon, and (c, e, g) C=O at depths of 300 µm, which is the top surface of the channel, 150 µm, which is the middle, and 0 µm, which is the bottom of the channel. (h) Secondary electron microscope image of a single channel whose tip was sliced using a sharp razor blade. EDS maps of (i) Silicon and (j) Carbon performed on the sliced tip. Scale bar in (a) is 200 µm.

Based on this work, it becomes evident irradiating a photo-reactive monomer-nanoparticle mixture under conditions which the light source undergoes self-trapping elicits organization of the formulation, directing the dynamics of phase separation dictates by the light profile over the entire depth. Microscopic flow induced due to the periodic nature of the light intensity would be expected to slightly distort the final morphology of the structures owing to interactions between the flowing monomer and projected light beams, also known as the congruency effect. The light beams are Gaussian in nature, with intensity highest at their center and lower spanning radially outward, the effect of which is reflected in the final, tapered/conical morphology of the structures. However, no significant difference between the macroscopic light pattern and the final morphology could be detected based on the optical microscopy and electron microscopy images. This alludes to the importance of the optical beams intensity to not only form the structure, but also mitigate any subsequent distortion during growth. Hence, light self-trapping in-turn governs the final morphology of the composite material, potentially revealing an important and useful correlation between irradiation intensity and morphology of the structures, the key link between the two being the competition between photopolymerization kinetics and drive of a system to phase-separate.

Further exploration elucidating the exact dynamics of phase-separation in such systems and length scales at which such behavior is possible is necessary and will be reported on in the future. For similar high-χ systems, we anticipate that more spatially coherent core-shell structures would result at even lower irradiation intensities, whereas the formation of purely embedded structures would entail the use of much higher irradiation intensity (examples for each case shown in Supporting Information). We also expect beam size to influence the final morphology of structures: smaller beams would reduce the diffusion path-length for nanoparticles to reach the beam periphery, facilitating quicker phase-separation and smaller feature sizes, whereas larger beams would vitrify the particles in larger sized structures due to the increased path-length to diffusion forming embedded structures. Examination of the correlation of morphology to such parameters as beam size, spacing, and other monomer-nanoparticle compositions (in addition to how they shift the intensity dependence ranges) is the subjective of current study.

CONCLUSION

We have demonstrated an intensity-dependent morphology in a photo-reactive monomer-nanoparticle formulation using non-uniform, visible light irradiation under conditions that allow for preservation (i.e., divergence-free) of the light profile over the sample of the formulation. In such highly immiscible systems, irradiation intensity plays an interactive role in controlling morphology evolution, and rate of polymer growth both further drives the system to phase separate, but also mitigates dynamics in the system owing to lower mobility with higher molecular weight. Thereby, the phase separated morphology may be allowed to proceed at low intensities, creating clear phase separated structures, or the phase separation is arrested at high intensities, creating structures with nanoparticles trapped (embedded) in the irradiated regions. Using in-situ Raman spectroscopy, the behavior of Si nanoparticles during irradiation at different intensities was monitored. Low irradiation intensity can be associated with increased nanoparticle mobility and formation of the phase-separated structures whereas high irradiation intensity was found to arrest nanoparticle mobility causing retardation of phase-separation. Characterization and quantitative analysis with 3D Raman volume and EDS mapping analysis further confirm the presence of phase-separated and arrested morphologies. This work provides a principle whereby the processing of monomer-nanoparticle formulations with large thicknesses (> 1mm) can control morphology over the entire depth, by controlling the degrees of segregation of the components. Further studies involving processing parameters such as beam size and mask size, as well as the influence of monomer functionality and nanoparticle weight fraction are currently in progress. Probing the effect of these parameters would expand the capability to control and tailor morphology over a range of structure parameters and compositions.

ACKNOWLEDGEMENTS

The authors gratefully acknowledge funding supported by the National Science Foundation under grant number CMMI-1751621, the 3M Foundation (NTFA) award, as well as support from the College of Engineering and Computer Science at Syracuse University.

SUPPORTING INFORMATION

Schematic of photopolymerization reaction (S1), schematic of Raman in-situ setup (S2), snapshot of laser beam position and photomask (S3), additional Raman in-situ data for other depths (S4-S5), Raman point spectra of samples before and after polymerization (S6-S7), Raman depth spectra before polymerization (S8-S9), extended kinetics data (S10), extended diffusion data (S11), full 3D Raman volume maps (S12-S13), supporting EDS mapping data with acquisition conditions and cross-sectional SEM and EDS maps (S14-S17), cross-sectional 3D Raman volume maps of supplementary control experiments (S18-S19), table of EDS intensities (Table S1), and table of representative values of conversion, molecular weight, viscosity and diffusion coefficients (Table S2).

REFERENCES

1. Hanemann, T.; Szabó, D. V., Polymer-Nanoparticle Composites: From Synthesis to Modern Applications. *Materials* **2010,** *3*, 3468-3517.
2. Mendes-Felipe, C.; Oliveira, J.; Etxebarria, I.; Vilas-Vilela, J. L.; Lanceros-Mendez, S., State-of-the-Art and Future Challenges of UV Curable Polymer-Based Smart Materials for Printing Technologies. *Advanced Materials Technologies* **2019,** *4*, 1800618.
3. Fouassier, J.-P.; Rabek, J. F., *Radiation Curing in Polymer Science and Technology*. Elsevier,: London, 1993; Vol. 1-4.
4. Paquet, C.; Kumacheva, E., Patterning Semiconductor Nanocrystals in Polymer Films. *Adv. Funct. Mater.* **2007,** *17*, 3105-3110.
5. Greener, J.; van der Loop, T. H.; Paquet, C.; Scholes, G.; Kumacheva, E., A Study of Simultaneous Patterning and Alignment of Semiconductor Nanorods via Polymerization-Induced Phase Separation. *Langmuir* **2009,** *25*, 3173-3177.
6. Smith, D. M.; Li, C. Y.; Bunning, T. J., Light-Directed Mesoscale Phase Separation via Holographic Polymerization. *J. Polym. Sci. B Polym. Phys.* **2014,** *52*, 232-250.
7. Biria, S.; Malley, P. P. A.; Kahan, T. F.; Hosein, I. D., Tunable Nonlinear Optical Pattern Formation and Microstructure in Cross-Linking Acrylate Systems during Free-Radical Polymerization. *J. Phys. Chem. C* **2016,** *120*, 4517-4528.
8. Qiu, L. Q.; Saravanamuttu, K., Optical self-trapping in a photopolymer doped with Ag nanoparticles: a single-step route to metallodielectric cylindrical waveguides. *J. Opt. Soc. Am. B* **2012,** *29*, 1085-1093.
9. Biria, S.; Wilhelm, T. S.; Mohseni, P. K.; Hosein, I. D., Direct Light-Writing of Nanoparticle-Based Metallo-Dielectric Optical Waveguide Arrays Over Silicon Solar Cells for Wide-Angle Light Collecting Modules. *Adv. Opt. Mater.* **2019,** *7*, 1900661.
10. Hosein, I. D., Light-Directed Organization of Polymer Materials from Photoreactive Formulations. *Chem. Mater.* **2020,** *32*, 2673-2687.
11. Biria, S.; Morim, D. R.; Tsao, F. A.; Saravanamuttu, K.; Hosein, I. D., Coupling nonlinear optical waves to photoreactive and phase-separating soft matter: Current status and perspectives. *Chaos* **2017,** *27*.
12. Kewitsch, A. S.; Yariv, A., Nonlinear optical properties of photoresists for projection lithography. *Appl. Phys. Lett.* **1996,** *68*, 455-457.
13. Yamashita, T.; Kagami, M.; Ito, H., Waveguide shape control and loss properties of light-induced self-written (LISW) optical waveguides. *J. Lightwave Technol.* **2002,** *20*, 1556-1562.
14. Kagami, M.; Yamashita, T.; Ito, H., Light-induced self-written three-dimensional optical waveguide. *Appl. Phys. Lett.* **2001,** *79*, 1079-1081.
15. Basker, D. K.; Brook, M. A.; Saravanamuttu, K., Spontaneous Emergence of Nonlinear Light Waves and Self-Inscribed Waveguide Microstructure during the Cationic Polymerization of Epoxides. *J. Phys. Chem. C* **2015,** *119*, 20606-20617.
16. Chen, F. H.; Pathreeker, S.; Biria, S.; Hosein, I. D., Synthesis of Micropillar Arrays via Photopolymerization: An in Situ Study of Light-Induced Formation, Growth Kinetics, and the Influence of Oxygen Inhibition. *Macromolecules* **2017,** *50*, 5767-5778.
17. Li, H.; Chen, F.-H.; Biria, S.; Hosein, I. D., Prototyping of Superhydrophobic Surfaces from Structure-Tunable Micropillar Arrays Using Visible Light Photocuring. *Advanced Engineering Materials* **2019,** *21*, 1801150.
18. Jacobsen, A. J.; Barvosa-Carter, W.; Nutt, S., Micro-scale truss structures formed from self-propagating photopolymer waveguides. *Adv. Mater.* **2007,** *19*, 3892-3896.
19. Lin, H.; Biria, S.; Chen, F.-H.; Hosein, I. D.; Saravanamuttu, K., Waveguide-imprinted slim polymer films: beam steering coatings for solar cells. *ACS Photonics* **2019,** *6*, 878-885.

20. Lin, H.; Hosein, I. D.; Benincasa, K. A.; Saravanamuttu, K., A Slim Polymer Film with a Seamless Panoramic Field of View: The Radially Distributed Waveguide Encoded Lattice (RDWEL). *Adv. Opt. Mater.* **2019,** *7*, 1801091.
21. Ponte, M. R.; Hudson, A. D.; Saravanamuttu, K., Self-Organized Lattices of Nonlinear Optochemical Waves in Photopolymerizable Fluids: The Spontaneous Emergence of 3-D Order in a Weakly Correlated System. *The Journal of Physical Chemistry Letters* **2018,** *9*, 1146-1155.
22. Hosein, I. D.; Lin, H.; Ponte, M. R.; Basker, D. K.; Brook, M. A.; Saravanamuttu, K., Waveguide Encoded Lattices (WELs): Slim Polymer Films with Panoramic Fields of View (FOV) and Multiple Imaging Functionality. *Adv. Funct. Mater.* **2017,** *27*, 1702242.
23. Ponte, M. R.; Welch, R.; Saravanamuttu, K., An optochemically organized nonlinear waveguide lattice with primitive cubic symmetry. *Opt. Express* **2013,** *21*, 4205-4214.
24. Kasala, K.; Saravanamuttu, K., Optochemical Organization in a Spatially Modulated Incandescent Field: A Single-Step Route to Black and Bright Polymer Lattices. *Langmuir* **2013,** *29*, 1221-1227.
25. Kasala, K.; Saravanamuttu, K., Optochemical self-organisation of white light in a photopolymerisable gel: a single-step route to intersecting and interleaving 3-D optical and waveguide lattices. *J. Mater. Chem.* **2012,** *22*, 12281-12287.
26. Burgess, I. B.; Ponte, M. R.; Saravanamuttu, K., Spontaneous formation of 3-D optical and structural lattices from two orthogonal and mutually incoherent beams of white light propagating in a photopolymerisable material. *J. Mater. Chem.* **2008,** *18*, 4133-4139.
27. Biria, S.; Chen, F.-H.; Hosein, I. D., Enhanced Wide-Angle Energy Conversion Using Structure-Tunable Waveguide Arrays as Encapsulation Materials for Silicon Solar Cells. *physica status solidi (a)* **2019,** *216*, 1800716.
28. Basker, D. K.; Cortes, O. A. H.; Brook, M. A.; Saravanamuttu, K., 3D Nonlinear Inscription of Complex Microcomponents (3D NSCRIPT): Printing Functional Dielectric and Metallodielectric Polymer Structures with Nonlinear Waves of Blue LED Light. *Advanced Materials Technologies* **2017**, 1600236-n/a.
29. Biria, S.; Hosein, I. D., Control of Morphology in Polymer Blends through Light Self-Trapping: An in Situ Study of Structure Evolution, Reaction Kinetics, and Phase Separation. *Macromolecules* **2017,** *50*, 3617–3626.
30. Biria, S.; Hosein, I. D., Superhydrophobic Microporous Substrates via Photocuring: Coupling Optical Pattern Formation to Phase Separation for Process-Tunable Pore Architectures. *ACS Appl. Mater. Interfaces* **2018,** *10*, 3094-3105.
31. Biria, S.; Hosein, I. D., Simulations of Morphology Evolution in Polymer Blends during Light Self-Trapping. *J. Phys. Chem. C* **2017,** *121*, 11717–11726.
32. Biria, S.; Chen, F. H.; Pathreeker, S.; Hosein, I. D., Polymer Encapsulants Incorporating Light-Guiding Architectures to Increase Optical Energy Conversion in Solar Cells. *Adv. Mater.* **2017,** *30*, 1705382.
33. Juhl, A. T.; Busbee, J. D.; Koval, J. J.; Natarajan, L. V.; Tondiglia, V. P.; Vaia, R. A.; Bunning, T. J.; Braun, P. V., Holographically Directed Assembly of Polymer Nanocomposites. *ACS Nano* **2010,** *4*, 5953-5961.
34. Decker, C., The use of UV irradiation in polymerization. *Polym. Int.* **1998,** *45*, 133-141.
35. Decker, C.; Moussa, K., Real-Time Kinetic-Study of Laser-Induced Polymerization. *Macromolecules* **1989,** *22*, 4455-4462.
36. Dendukuri, D.; Panda, P.; Haghgooie, R.; Kim, J. M.; Hatton, T. A.; Doyle, P. S., Modeling of Oxygen-Inhibited Free Radical Photopolymerization in a PDMS Microfluidic Device. *Macromolecules* **2008,** *41*, 8547-8556.
37. Kewitsch, A. S.; Yariv, A., Self-focusing and self-trapping of optical beams upon photopolymerization. *Opt. Lett.* **1996,** *21*, 24-26.
38. Bauer, B. J.; Briber, R. M., The effect of crosslink density on phase separation in interpenetrating polymer networks. In *Advances in interpenetrating polymer networks*, Klempner, D.; Frisch, K., Eds. CRC Press: Lancaster, PA, 1994; Vol. 4, p 45.

39. Flory, P. J.; Rehner, J., Statistical mechanics of cross-linked polymer networks II Swelling. *J. Chem. Phys.* **1943,** *11*, 521-526.
40. Flory, P. J., *Principles of Polymer Chemistry*. Cornell University Press: Ithaca, 1953.
41. Nakano, H.; Nakamura, D., Hansen Solubility Parameters of Stacked Silicanes Derived from Porous Silicon. *ACS Omega* **2019,** *4*, 11838-11843.
42. Lekkerkerker, H. N.; Poon, W.-K.; Pusey, P. N.; Stroobants, A.; Warren, P., Phase behaviour of colloid+ polymer mixtures. *EPL (Europhysics Letters)* **1992,** *20*, 559.
43. Ilett, S.; Orrock, A.; Poon, W.; Pusey, P., Phase behavior of a model colloid-polymer mixture. *Phys. Rev. E* **1995,** *51*, 1344.
44. Kim, J.; Cho, C.; Palffy-Muhoray, P.; Kyu, T., Polymerization-induced phase separation in a liquid-crystal-polymer mixture. *Phys. Rev. Lett.* **1993,** *71*, 2232.
45. Gögelein, C.; Nägele, G.; Buitenhuis, J.; Tuinier, R.; Dhont, J. K., Polymer depletion-driven cluster aggregation and initial phase separation in charged nanosized colloids. *The Journal of chemical physics* **2009,** *130*, 204905.
46. Chung, H.-J.; Taubert, A.; Deshmukh, R.; Composto, R. J., Mobile nanoparticles and their effect on phase separation dynamics in thin-film polymer blends. *EPL (Europhysics Letters)* **2004,** *68*, 219.
47. Ramakrishnan, S.; Fuchs, M.; Schweizer, K. S.; Zukoski, C. F., Entropy driven phase transitions in colloid–polymer suspensions: Tests of depletion theories. *The Journal of chemical physics* **2002,** *116*, 2201-2212.
48. Kryven, I.; Duivenvoorden, J.; Hermans, J.; Iedema, P. D., Random Graph Approach to Multifunctional Molecular Networks. *Macromol Theor Simul* **2016,** *25*, 449-465.
49. Flory, P. J., Molecular size distribution in three dimensional polymers. I. Gelation1. *J. Am. Chem. Soc.* **1941,** *63*, 3083-3090.
50. Lecamp, L.; Youssef, B.; Bunel, C.; Lebaudy, P., Photoinitiated polymerization of a dimethacrylate oligomer: 2. Kinetic studies. *Polymer* **1999,** *40*, 1403-1409.
51. Anseth, K. S.; Wang, C. M.; Bowman, C. N., Kinetic evidence of reaction diffusion during the polymerization of multi (meth) acrylate monomers. *Macromolecules* **1994,** *27*, 650-655.
52. Zywietz, U.; Evlyukhin, A. B.; Reinhardt, C.; Chichkov, B. N., Laser printing of silicon nanoparticles with resonant optical electric and magnetic responses. *Nat. Commun.* **2014,** *5*, 3402.
53. Meier, C.; Gondorf, A.; Lüttjohann, S.; Lorke, A.; Wiggers, H., Silicon nanoparticles: Absorption, emission, and the nature of the electronic bandgap. *J Appl Phys* **2007,** *101*, 103112.
54. Anseth, K. S.; Wang, C. M.; Bowman, C. N., Reaction behaviour and kinetic constants for photopolymerizations of multi(meth)acrylate monomers. *Polymer* **1994,** *35*, 3243-3250.
55. Furubayashi, Y.; Kawakubo, R.; Nakanishi, H.; Norisuye, T.; Tran-Cong-Miyata, Q., Effects of the positive feedback loop in polymerization on the reaction-induced phase separation of polymer mixtures. *Chaos* **2015,** *25*.
56. Ozaki, T.; Koto, T.; Nguyen, T. V.; Nakanishi, H.; Norisuye, T.; Tran-Cong-Miyata, Q., The roles of the Trommsdorff-Norrish effect in phase separation of binary polymer mixtures induced by photopolymerization. *Polymer* **2014,** *55*, 1809-1816.
57. Hiemenz, P. C.; Lodge, T. P., *Polymer Chemistry, Second Edition*. Taylor & Francis: 2007.
58. Billmeyer Jr., F. W., Methods for estimating intrinsic viscosity. *Journal of Polymer Science* **1949,** *4*, 83-86.
59. Pamies, R.; Hernández Cifre, J. G.; del Carmen López Martínez, M.; García de la Torre, J., Determination of intrinsic viscosities of macromolecules and nanoparticles. Comparison of single-point and dilution procedures. *Colloid Polym Sci* **2008,** *286*, 1223-1231.
60. Slark, A. T.; Sherrington, D. C.; Titterton, A.; Martin, I. K., Branched methacrylate copolymers from multifunctional comonomers: the effect of multifunctional monomer functionality on polymer architecture and properties. *J. Mater. Chem.* **2003,** *13*, 2711-2720.
61. Yamamoto, U.; Schweizer, K. S., Theory of nanoparticle diffusion in unentangled and entangled polymer melts. *The Journal of Chemical Physics* **2011,** *135*, 224902.

62. Grabowski, C. A.; Mukhopadhyay, A., Size Effect of Nanoparticle Diffusion in a Polymer Melt. *Macromolecules* **2014,** *47*, 7238-7242.
63. Kohli, I.; Mukhopadhyay, A., Diffusion of Nanoparticles in Semidilute Polymer Solutions: Effect of Different Length Scales. *Macromolecules* **2012,** *45*, 6143-6149.
64. Liu, J.; Cao, D.; Zhang, L., Molecular Dynamics Study on Nanoparticle Diffusion in Polymer Melts: A Test of the Stokes−Einstein Law. *J. Phys. Chem. C* **2008,** *112*, 6653-6661.

FOR TABLE OF CONTENTS USE ONLY